Deep-Learning-Assisted Resonant Ultrasound Spectroscopy for Cubic Solids

Hiroki Fukuda,[1] Akira Nagakubo,[1] Oliver B. Wright,[1,2] Kazuhiro Kyotani,[3] and Hirotsugu Ogi[1,*]

[1] *Graduate School of Engineering, Osaka University, Yamadaoka 2-1, Suita, Osaka 565-0871, Japan*
[2] *Hokkaido University, Sapporo 060-0808, Japan*
[3] *Insight K. K., 2-6-7 Hyakunincho, Shinjuku-ku, Tokyo 169-0073, Japan*

(Received 7 June 2023; revised 7 August 2023; accepted 17 August 2023; published 21 September 2023)

This paper solves a long-standing problem in resonant ultrasound spectroscopy (RUS) for cubic solids through the use of two-dimensional deep learning (DL). By means of inverse methods, conventional RUS can determine all independent elastic constants of a crystalline solid specimen by comparing measured and calculated free-vibration resonance frequencies. However, to avoid invalid local minima in the inverse process, good initial guesses of the elastic constants must be available. Here, we propose a DL scheme to remedy this problem, which utilizes an input elasticity image composed of three layers obtained from resonance frequency data. After network training, this scheme is executed in two steps: DL processing by a neural network to output elastic constants in a Blackman diagram classification, followed by the use of a regression network around the classified point in this diagram for more accurate determination. By means of simulations, we demonstrate that this DL scheme yields the principal elastic constants within an error of approximately 5% without any inverse processing even in the unfavorable case of five missing modes for 111 existing cubic crystals.

DOI: 10.1103/PhysRevApplied.20.034048

I. INTRODUCTION

The elastic constants of a material are related to a broad range of physical properties because they are used in the material's equation of state [1]. They are also crucial for assessing the reliability of theoretical calculations [2–4]. The accurate measurement of these constants remains an issue in condensed-matter physics. For solids that can be cut into regular shapes, such as a sphere, cylinder, or rectangular parallelepiped, resonant ultrasound spectroscopy (RUS) is a powerful method for determining all independent elastic constants C_{ij} [5–9]. This method involves measuring a number of free-vibration resonance frequencies of the specimen and then, by an inverse method, such as the nonlinear least-squares optimization method based on the Levenberg-Marquardt algorithm, extract a set of C_{ij} that closely matches the measured resonance frequencies.

Although the RUS method is superior to other methods for accurately measuring the C_{ij} of small specimens on a millimeter or submillimeter scale [10], it has several drawbacks that have not been fully resolved. Firstly, one must do a complex mathematical eigenvalue extraction. Secondly, the inverse method requires an arduous code-development process, only accessible by specialists. Thirdly, there remains an inherent difficulty in mode identification. Correct identification is required between the measured and calculated resonance frequencies. Misidentification of modes causes the inverse calculation to converge to a local minimum, resulting in a physically meaningless answer. Missing modes in the measurements thus make the mode-identification procedure highly labyrinthine. To avoid such misidentification, a sufficiently good initial guess is needed for the set C_{ij} at the beginning of the inverse calculation, which requires approximate values of C_{ij} to be known in advance. Because of these demands, the RUS method has remained an *ad hoc* method.

Various methods have been proposed to alleviate some of these problems. They include using different sized specimens [6], changing the frequency assignment during the iteration calculation [7], exploiting the dependence of the signal amplitude on the specimen orientation relative to the transducers [8], controlling magnetic field direction for mode-selective excitation using electromagnetic acoustic transducers [11,12], and vibrational-pattern imaging with laser-Doppler interferometry of the resonating specimen [13–16]. In particular, vibrational-pattern imaging is performant in that it can completely identify modes by comparison of measured and calculated images. However, this technique requires long measurement times, sophisticated equipment, and intensive use of elasticity theories and complex analysis. And the other methods involve

*ogi@prec.eng.osaka-u.ac.jp

laborious extra steps. There is therefore still no quick and easy method that can reliably provide the correct set C_{ij}. In a nutshell, the RUS resonance spectrum is essentially a forest of resonances with a unique signature like a barcode that needs to be deciphered. The problem is that it is very hard to decipher.

Here, we propose a three-layer two-dimensional deep-learning (3L2DDL) neural-network methodology in RUS for determining the set C_{ij} of cubic solids without the need for mode identification. Such machine learning has been recently adopted in RUS to determine elastic constants from jumps in resonant frequencies at phase transitions [17] or from the resonant frequencies of piezoelectric materials [18] using one-dimensional (1D) methods. However, these are limited to specific cases, do not tolerate missing modes, and are not suitable for application to a whole class of elastic materials, as one often does not always know approximate elastic constants of a specimen in advance, even if x-ray diffraction, for example, has confirmed its crystal structure. Two-dimensional machine-learning methods, i.e., 2DDL, were reported to be superior to 1DDL for the case of recognition of protein secondary structures [19]. In this paper, we report a 3L2DDL method that can solve all of the above problems in RUS, in particular, that of the requirement for initial guesses of the elastic constants. Moreover, we demonstrate that the method is insensitive to the thorny problem of missing modes, and, crucially, is applicable to the whole class of all known cubic symmetry materials.

Our method extracts all elastic constants C_{ij} close to the true values by use of three-layer image datasets, also viewable as a single RGB image in each case for convenience (although this does not contain all the information in the original three layers, e.g., concerning which layer has which binary value), by means of the following steps. First, the neural network is trained from a set of RGB elasticity images generated from a large number of known virtual cubic materials, classified by use of a Blackman diagram, i.e., a plot of C_{44}/C_{11} against C_{12}/C_{11} [20]—a diagram widely used for cubic materials [21]. Each calculated RGB image is assigned a class based on the region, associated with a grid point, that it occupies on a specific Blackman diagram. Secondly, we derive the RGB image of the specimen under investigation from its resonance spectrum, assigning it using the neural network to the correct region on the appropriate Blackman diagram. Thirdly, regression of the set of C_{ij} is conducted in the region in question by means of a second 3L2DDL network. This finds the set C_{ij} that corresponds to the input RGB image. To demonstrate the reliability of the method, we apply our DL scheme to >100 actual cubic materials, demonstrating unprecedentedly efficient C_{ij} determination in RUS. In short, *without the use of any inverse methods*, we determine C_{ij} with an accuracy of 95% or higher, even in the case of five missing modes. Furthermore, by performing a standard inverse calculation used in RUS methods using the C_{ij} predicted with our DL scheme as initial guesses, one can obtain a very accurate result.

II. DATASET PREPARATION

A. Three-layer elasticity image

Most of the focus in this paper concerns simulations for a specimen in the shape of a rectangular parallelepiped specimen with sides in the ratio 3:4:5. This shape is often used in performing RUS measurements, and is considered to be generic in the field. Deviations from these chosen ratios do not significantly affect the classification and regression results, as demonstrated later. We choose a sample with these side ratios as a *reference* specimen: a rectangular parallelepiped cut parallel to the three principal axes of the cubic lattice to have sides 3, 4, and 5 mm.

Our approach relies on making images from resonance-frequency data for easier and more natural processing by the DL method. For a rectangular parallelepiped specimen, the parameter

$$\tilde{C}_n = \tilde{V}^{\frac{2}{3}} \rho {f_n}^2 \tag{1}$$

is chosen for purposes of construction of such an elasticity image for a particular specimen from its resonant frequencies f_n (where $n = 1, 2, 3 \cdots$). Here, ρ and f denote the mass density and each free-vibration resonance frequency, respectively, and $\tilde{V}$ denotes the ratio of the specimen volume under investigation to that of the reference specimen. This definition assures that $\tilde{C}$ depends only on the set C_{ij}, independent of the mass density and specimen size (see the Supplemental Material [22]). Figure 1 schematically explains the construction of the elasticity image, composed of three layers, each of which is made up of 15×15 pixels. One pixel corresponds to one value of $\tilde{C}$, and its argument takes one of two values, i.e., representing a binary variable. We make two assumptions:

(1) $\tilde{C}$ is chosen to range from 100 to 13,000 TPa m^{-2} when $\tilde{V} = 1$. The lower limit of 100 is chosen because it is close to the fundamental resonance frequency (f_1) of very soft materials, but does not exclude this frequency. The upper limit is high enough to encompass enough resonances for accurately distinguishing materials.

(2) n is chosen to range from from 1 to 100, i.e., making use of 100 resonance frequencies within this range of $\tilde{C}$. The limit prescribed by (1) ensures that all of the 100 resonances lie in the range of $\tilde{C}$ for all materials occurring in nature.

For example, in the case of a copper specimen of the reference size, this corresponds to the frequency range 0.106 and 1.206 MHz, where the fundamental ($n = 1$) and 100th resonance modes occur at 0.20 and 0.96 MHz, respectively. Even when a large number of resonance modes are observed, as is common in RUS experiments, not many

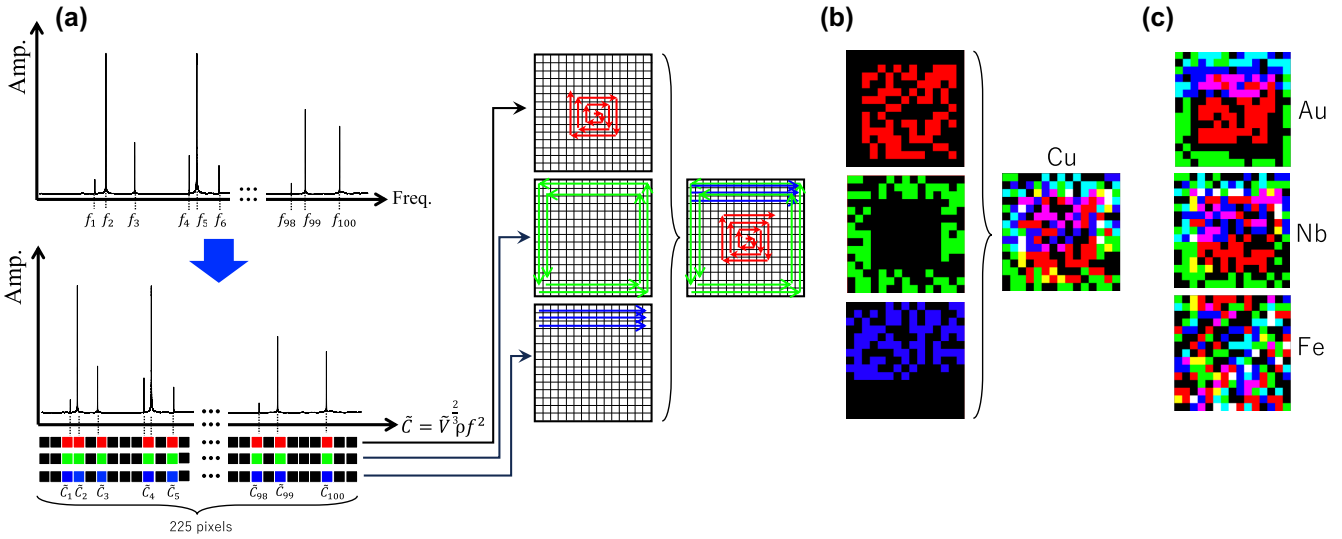

FIG. 1. Construction of the three-layer elasticity image. (a) Conversion of measured resonance frequencies to arguments of 225 pixels labeled according to the elasticity parameter $\tilde{C}_n$ over a predefined frequency range. (b) Construction of three layers for the case of single-crystal copper. This material is different from that shown in (a). Yellow, magenta, light blue, and white pixels result from the overlapping of red and green, red and blue, green and blue, and red, green, and blue pixels, respectively. (c) Elasticity images for gold, niobium, and iron. Freq. is an abbreviation for frequency.

resonance frequencies can be used for the standard inverse calculation because of the difficulty in mode identification for higher-order modes. Since our elasticity image does *not* require mode identification, such higher-order resonance modes, in contrast, play a key role in our analysis.

Dividing up the range of $\tilde{C}$ values into 225 equal intervals, we map binary information concerning the presence (1) or absence (0) of a resonance in each interval onto images of $15 \times 15 = 225$ pixels, but with the proviso that only the first 100 resonances in this interval are used—the rest outside the prescribed range being ignored [see Fig. 1(a)]. Use of 225 pixels is found not to degrade the fidelity of the whole process: rather it improves the classification accuracy or leaves it unaffected.

As mentioned above, three images, or layers, are created, each with 225 values of binary data, but a different mapping process is used for each layer. For the first layer (the "red" layer), the binary values are spirally (clockwise) distributed from the center outwards, a red pixel representing 1 and black pixel representing 0; in the second layer (the "green" layer), the binary values are spirally (clockwise) distributed from the outside inwards towards the center, starting from the bottom left edge; in the third layer (the "blue" layer), the binary values are horizontally distributed (i.e., as in a raster scan) from the top side downwards, starting from the top-left edge. This process is shown in Fig. 1(b) for the example of copper. Extended black areas in the three layers arise because of stipulation (2) above, i.e., the use of only the first 100 resonances in the precised interval in (1) above. The three layers of 225 pixels with purely binary data for each pixel represent the input data for the DL processing, but for ease of viewability we combine them into a single color image that represents the cubic material in a single frame. Yellow, magenta, light blue, and white pixels result from the overlap of red and green, red and blue, green and blue, and red, green and blue pixels, respectively. An example of elastic image construction is shown in Fig. 1(c) for the cases of gold, niobium, and iron.

Such an elastic image represents the elastic properties of a material. For a soft material, where the elasticity parameter takes smaller values, red pixels are distributed near the center, green pixels near the periphery, and blue pixels near the top region, resulting in an image with little overlap between pixels [as in the example of gold in Fig. 1(c)]. On the other hand, for a stiffer material, pixels of each color are distributed throughout the image, resulting in many overlapping pixels [as in the examples of iron in Fig. 1(c)]. In this ansatz, overlap between pixels is clearly a factor that represents the elasticity of the material. This is the motivation for the proposed image-coding scheme. As shown later, the three-layer elasticity image we propose shows high tolerance to the presence of missing modes compared with other inputs.

B. Classification on the Blackman diagram

The first step of the 3L2DDL scheme requires neural-network training. To this end we classify each input elasticity image on the Blackman diagram, where both axes range from 0 to 1. Involving the entire area of the Blackman diagram in the classification scheme would increase computation time. We therefore restrict the area to be examined

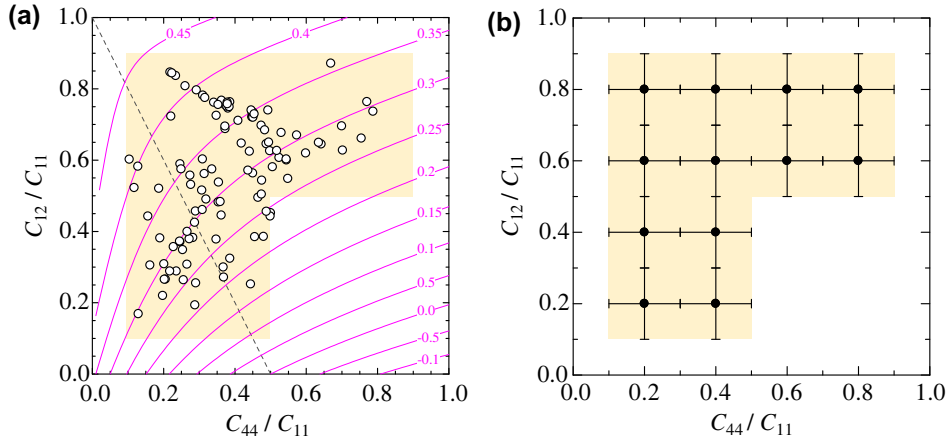

FIG. 2. Classification on the Blackman diagram. (a) Plots of reported cubic materials on the Blackman diagram (open circles). Red curves indicate Poisson's ratio and the broken line indicates the isotropic material case. The shaded area is considered for making the datasets. (b) 12 classes (solid circles) set on the Blackman diagram at each C_{11} value. The error bars indicate the stiffness blurring used for preparing the datasets.

to the region where actual materials exist. Figure 2(a) shows plots on the Blackman diagram for 111 real cubic materials (see the Supplemental Material), suggesting that materials that can exist in nature are expected to appear in the shaded area in Fig. 2(a). This area occupies 48% of the entire area.

We choose 12 regions for classification within the chosen area, each a square with one side equal to 0.2, indicated by black circles that occupy their central (i.e., lattice) points, as shown in Fig. 2(b): C_{11} is divided into steps of 25 GPa between 50 and 450 GPa, and for each of these 17 C_{11} values there is a corresponding Blackman diagram. Since each C_{11} value gives rise to 12 lattice points on the diagram, the number of total classes is equal to $12 \times 17 = 204$. This relatively large number of classes is beneficial for a reasonably accurate determination of the elastic constants without the use of an inverse method.

Because the eigenfrequencies of the reference specimen can be calculated with sufficient accuracy according with the Ritz method, based on normalized Legendre polynomials, by increasing the polynomial order (see the Supplemental Material [22]) [23], we can numerically construct elasticity images for individual sets of C_{ij} for purposes of training the neural network. For each class, we prepare such images by randomly introducing errors in the elastic constants up to ± 12.5 GPa for C_{11} and up to ± 0.1 for C_{44}/C_{11} and C_{12}/C_{11}, as indicated by the error bars in Fig. 2(b). To investigate the sensitivity to missing modes that occur in experiment, we also randomly removed up to five resonance modes. By introducing such "blurring" and artificial measurement errors into the training datasets, the resultant neural networks become more robust to errors in specimen dimensions and to missing modes. The number of training datasets at each class is 18 000, resulting in a total number of 3 672 000 datasets used.

III. THREE-LAYER TWO-DIMENSIONAL DEEP-LEARNING SCHEME

An input elasticity image is first classified into one of the 204 classes on the Blackman diagram by use of the convolutional neural network constructed in this study, as shown in Fig. 3(a). It consists of an input layer for the three-layer elastic image of 15×15 pixels, which is followed by a 2D convolution layer and a batch-normalization layer. After the Subnetwork Unit [see Fig. 3(b)] is repeated 6 times, the rectified linear-unit layer, the 2D max pooling layer, the 2D convolution layer and the batch-normalization layer are connected. The Subnetwork Unit is then repeated 6 times, followed by the rectified linear-unit-activation layer, dropout layer, fully connected layer for classification, softmax layer, and then finally the classification output layer. The structure of the Subnetwork Unit is shown in Fig. 3(b), where we introduce two shortcut connections, allowing a very deep network with hundreds of layers [24]. The elasticity image is input to the classification network, which outputs for each class the probability to which the image belongs. For most input images, only one of the 204 classes is output with almost 100% probability, but for some input images, multiple classes are output with high probability. Therefore, classes with the classification probability of 5% or higher are selected as possible classes to which the input elasticity image may belong.

Second, the input elasticity image is used to predict the set of C_{ij} in the vicinity of the classes indicated in the first classification step, using the same datasets of those selected classes. We construct a different neural network for this regression scheme, as shown in Fig. S1 within the Supplemental Material [22].

First and second 3L2DDL networks are trained with an adaptive-moment-estimation (Adam) optimizer using

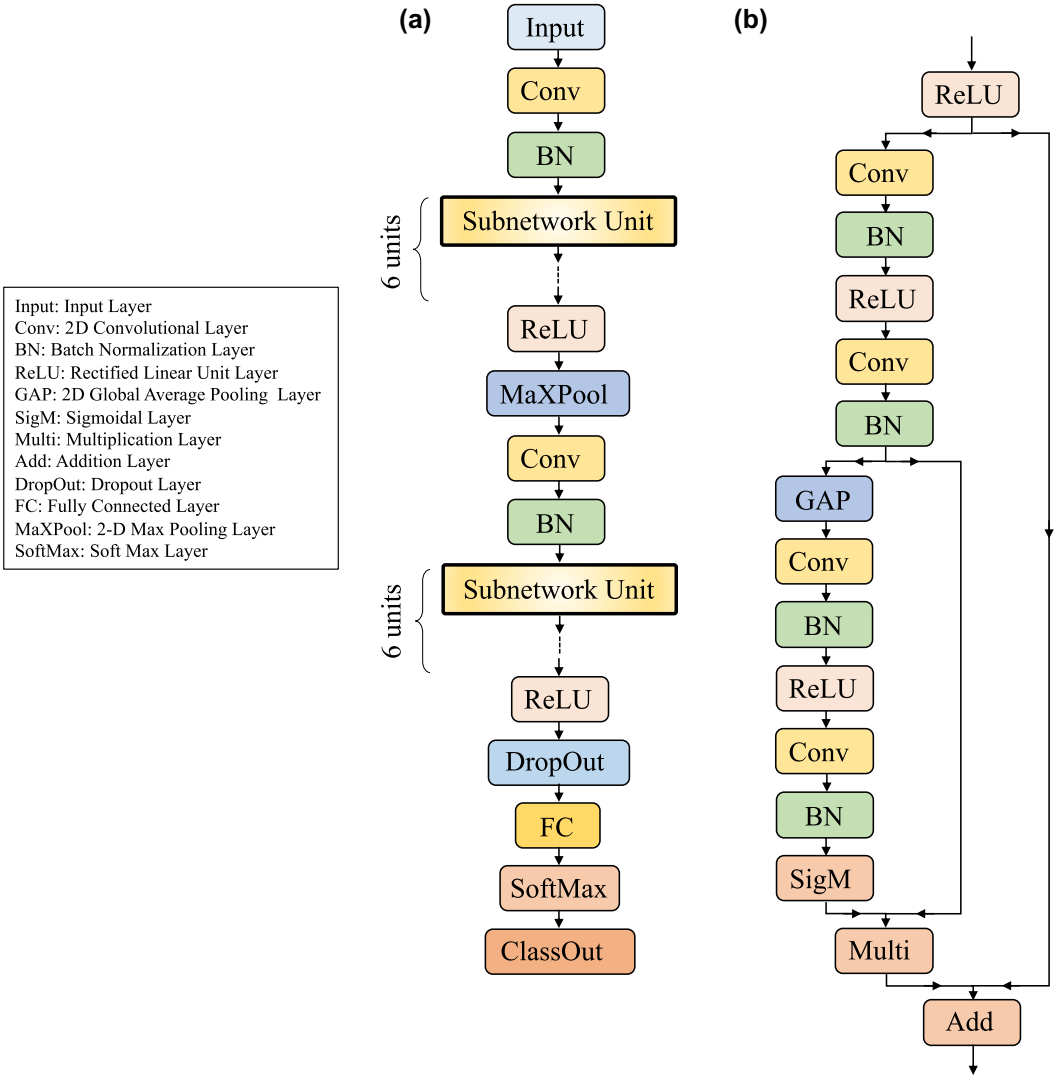

FIG. 3. Three-layer two-dimensional deep-learning (3L2DDL) network for classification. (a) Overall structure of the 3L2DDL network, and (b) structure of the Subnetwork Unit.

MATLAB (R2022b). 99% of the datasets are used for training and 1% for validation for the classification network, and 90% for training and 10% for validation for the regression network. Their convergence behavior during training is shown in Figs. S2(a) and (b), respectively (see Supplemental Material [22]). The training accuracy exceeds 80%, and the validation accuracy is 71% for classification. The relatively low validation accuracy is caused by the artificial incorporation of errors in C_{ij} and by missing modes, both being necessary to improve the network's tolerance to material variation and to dimensional errors.

IV. RESULTS AND DISCUSSION

We first investigate the tolerance of our 3L2DDL network to the presence of missing modes. This often happens in experiment when the point of the contact of the transducer with the specimen surface is close to the nodal line of the resonant mode. Our elasticity image ansatz is less affected by missing modes, because the absence of a resonance mode only blackens a single pixel in each layer, but does not significantly affect the overall image. For example, Fig. 4(a) shows elasticity images of Si containing up to 10 missing modes. Our classification network is in fact able to classify elastic images with up to six missing modes into the correct classes. Even with ten missing modes, 80% classification accuracy is achieved. The more accurately regression-derived elastic constants turn out to be less sensitive to the missing modes, as shown in Fig. 4(b); even with ten missing modes, the principal elastic constants C_{11}, C_{44}, and E_1 are predicted to fair accuracy (where E_1 denotes the Young modulus along the principal axis of the cubic material). Thus, the three-layer elasticity

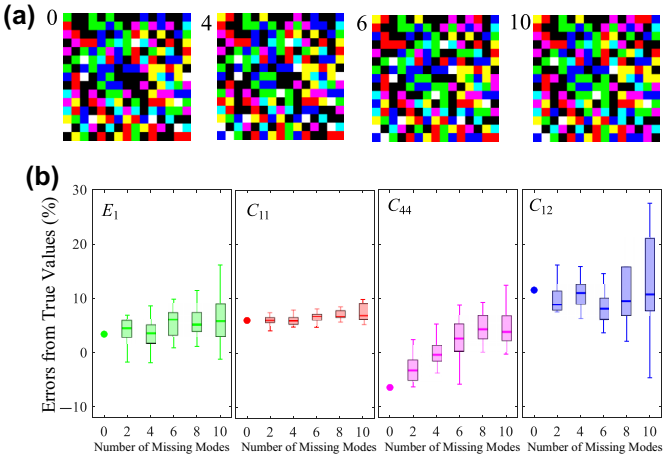

FIG. 4. (a) Elasticity images for Si involving 0, 4, 6, 10 missing modes, and (b) box plots showing the difference between regression-derived and true elastic constants with up to ten missing modes.

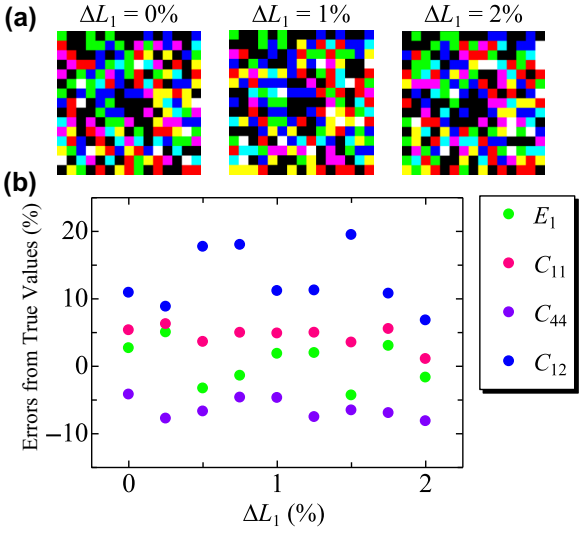

FIG. 5. (a) Elasticity images of Si with dimension errors of 0, 1, and 2% in the longest side. (b) Difference between regression-derived and true elastic constants with the dimension errors up to 2%.

image we propose shows high tolerance to the presence of missing modes, and it is significantly superior to other possible inputs, such as the use of a one-layer binary image or one-layer eight-bit image, as demonstrated in Fig. S4 (see the Supplemental Material [22]).

Next, we discuss the influence of the error in the dimensions. As mentioned above, the RUS method using rectangular parallelepiped specimens requires cutting an appropriate sample, and preparation of a specimen with the 3:4:5 dimensional ratio is relatively straightforward. However, some deviation from this ratio is to be expected. Figure 5 shows elasticity images for Si when a dimensional error is introduced to the reference sample on the longest side. These results indicate that such an error up to 2% will not have a significant influence on elastic constant prediction on our 3L2DDL network alone. (More accurate C_{ij} can be output by standard inverse calculations based on initial C_{ij} predicted by the 3L2DDL scheme using known sample dimensions.) This tolerance to errors in dimension is thanks to the incorporation of artificial errors in the training datasets. Even if the dimensional ratio deviates strongly from that of the reference specimen, accurate estimation of C_{ij} can be achieved by creating datasets for the dimensional ratio in question. At present, dataset preparation and subsequent training take approximately 2 days for a desktop PC (CPU: Intel Core, i9-12900K, 16 cores, 3.2 GHz, 2.4 GHz, RAM: Crucial DDR4 64 GB, 3200 MHz, GPU: Nvidia Geforce RTX 3090, RAM 24 GB).

We also confirmed that our 3L2DDL scheme is tolerant to measurement error in the resonant frequency, as

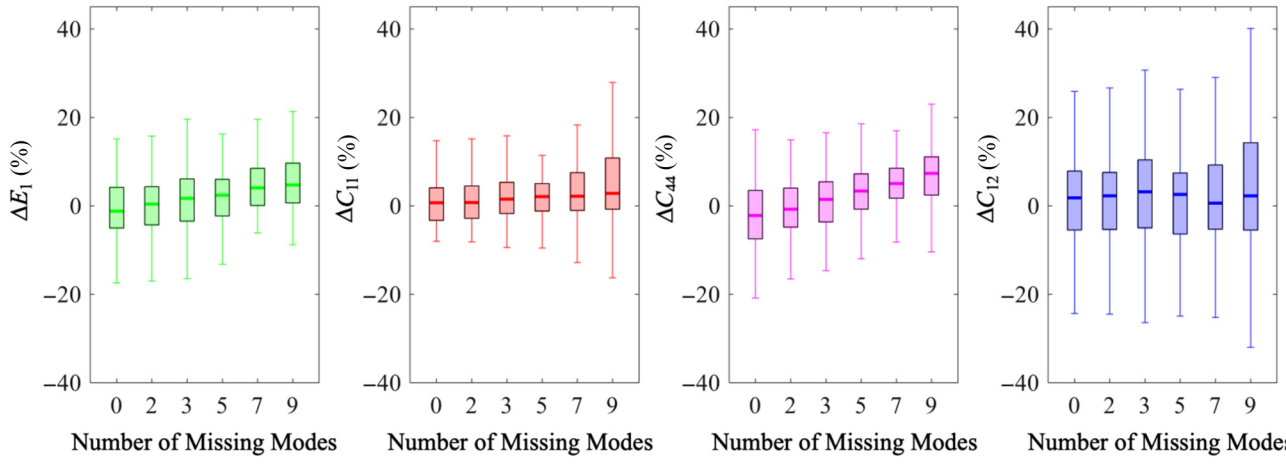

FIG. 6. Box plots for comparison between regression-calculated elastic constants by the 3L2DDL method and reported values for 111 cubic materials with up to nine missing modes.

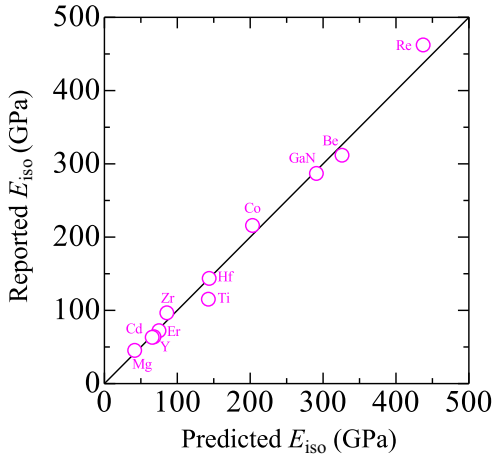

FIG. 7. Application to hexagonal materials: comparison between the average (isotropic) Young modulus E_{iso} calculated using five independent elastic constants from the literature with that using three elastic constants obtained by the regression process for various hexagonal materials.

demonstrated in Fig. S3 (see Supplemental Material [22]), where the measurement errors are artificially and randomly introduced based on a Gaussian distribution. The predicted elastic constants are nearly the same as those without the frequency error for root-mean-square frequency errors $<$ 0.5%, whereas the prediction accuracy deteriorates with errors $>$ 1%. In conventional RUS experiments, the resonant frequencies are very accurately determined with errors $<$ 0.1% [25], and so the measurement error should definitely not affect the prediction of the elastic constants using our 3L2DDL scheme.

The regression accuracy of the C_{ij} for 111 existing cubic materials [26–88] predicted by the 3L2DDL networks is shown in Fig. 6, and individual details are shown in Tables S1–S6. (References for their elastic constants are shown in Table S7.) Although the prediction accuracy for the off-diagonal component C_{12} is approximately 10% because of its lower contribution to the resonance frequencies, the principal components C_{11}, C_{44}, and E_1 agree with the true values to within approximately 5%, even though nine modes are missing. (Note that more than six missing modes are not included in the datasets and are not trained, but the elastic constants are accurately predicted.) This implies that these elastic constants can be determined with an error of less than 5% simply by measuring the resonance frequencies, without performing the inverse calculation at all, which corresponds to a tremendous simplification in RUS.

Finally, we discuss the applicability of our 3L2DDL scheme to lower symmetry materials. As an example, consider hexagonal materials, which exhibit five independent elastic constants. (Their elastic constants are shown in Table S8 [89–96].) The datasets used for training our neural networks do not include any hexagonal materials. Nevertheless, the elastic images can be constructed using their resonant frequencies to predict three elastic constants for various hexagonal materials. Although it may seem that there is no physical significance in determining three elastic constants for a hexagonal material that possesses five elastic constants, we find that the *average* elasticity properties are reproduced well. Figure 7 compares the Young modulus calculated by the Hill averaging method [97] using literature values and that using the DL-predicted three elastic constants. Their agreement suggests that the elasticity image we propose reflects the essential elastic properties of a material, and indicates that this scheme can be usefully applied to lower-symmetry solids.

V. CONCLUSIONS

In conclusion, we propose a two-dimensional deep-learning network scheme for determining the three independent elastic constants of cubic solids using their free-vibration resonant frequencies without performing the inverse calculation. The DL neural network is trained using the results of simulating RUS data for a set of known cubic materials each in the form of a rectangular parallelepiped with close to a 3:4:5 side ratio. Each RUS resonance spectrum is coded as a three-layer 15 $\times$ 15 pixel color input image, which is classified on a Blackman diagram. After training, the RUS spectrum for a cubic sample with unknown elastic constants can be used to produce an input image, which is then classified on a Blackman diagram. A regression network can then provide the elastic constants to $<\sim$ 5% error for the principal components. The accuracy of the resultant elastic constant determination is little affected by up to six missing modes, specimen dimension errors up to 2%, and the measurement errors on the resonance frequency up to 1%. We verified that applying the method to 111 existing cubic solids yields their elastic constants with the expected $<$ 5% error without any inverse calculation. The DL scheme is also shown to be applicable to hexagonal-symmetry materials, even though the neural-network training was only conducted on cubic materials. The method yields the average Young's modulus to reasonable accuracy, suggesting that our proposed elasticity images faithfully reflect material elastic properties. Our approach replaces what essentially has been a 1D barcode for coding a resonance spectrum by a 2D color image, somewhat analogously to the way QR codes can now replace barcodes in utility.

More work remains to further improve the accuracy of DL techniques in RUS, possibly by refining the input image format, and by extension to the derivation of elastic constants in lower symmetry crystal systems. However, already the ability to extract reasonably accurate elastic constants without heavy mathematical inverse techniques and in the presence of the invariable missing modes should revolutionize the field of elastic constant determination. This advancement is expected to have a significant impact

not only in solid-state physics but also in engineering, materials science, mineralogy, and geology.

[1] O. L. Anderson, *Equations of State of Solids for Geophysics and Ceramic Science* (Oxford University Press, Oxford, 1995).

[2] A. Nagakubo, H. Ogi, H. Sumiya, K. Kusakabe, and M. Hirao, Elastic constants of cubic and wurtzite boron nitrides, Appl. Phys. Lett. **102**, 241909 (2013).

[3] S. Lebègue, J. Harl, T. Gould, J. G. Ángyán, G. Kresse, and J. F. Dobson, Cohesive Properties and Asymptotics of the Dispersion Interaction in Graphite by the Random Phase Approximation, Phys. Rev. Lett. **105**, 196401 (2010).

[4] K. Kusakabe, A. Wake, A. Nagakubo, K. Murashima, M. Murakami, K. Adachi, and H. Ogi, Interplanar stiffness in defect-free monocrystalline graphite, Phys. Rev. Mater. **4**, 043603 (2020).

[5] H. H. Demarest, Cube-resonance method to determine the elastic constants of solids, J. Acoust. Soc. Am. **49**, 768 (1971).

[6] I. Ohno, Free vibration of a rectangular parallelepiped crystal and its application to determination of elastic constants of orthorhombic crystals, J. Phys. Earth **24**, 355 (1976).

[7] J. D. Maynard, The use of piezoelectric film and ultrasound resonance to determine the complete elastic tensor in one measurement, J. Acoust. Soc. Am. **91**, 1754 (1992).

[8] A. Migliori, J. Sarrao, W. M. Visscher, T. Bell, M. Lei, Z. Fisk, and R. Leisure, Resonant ultrasound spectroscopic techniques for measurement of the elastic moduli of solids, Phys. B: Condens. Matter **183**, 1 (1993).

[9] O. Svitelskiy, A. V. Suslov, J. B. Betts, A. Migliori, G. Yong, and L. A. Boatner, Resonant ultrasound spectroscopy of $KTa_{1-x}Nb_xO_3$ ferroelectric relaxor crystals, Phys. Rev. B **78**, 064113 (2008).

[10] H. Ledbetter, C. Fortunko, and P. Heyliger, Orthotropic elastic constants of a boron-aluminum fiber-reinforced composite: An acoustic-resonance-spectroscopy study, J. Appl. Phys. **78**, 1542 (1995).

[11] H. Ogi, H. Ledbetter, S. Kim, and M. Hirao, Contactless mode-selective resonance ultrasound spectroscopy: Electromagnetic acoustic resonance, J. Acoust. Soc. Am. **106**, 660 (1999).

[12] H. Ogi, S. Kai, H. Ledbetter, R. Tarumi, M. Hirao, and K. Takashima, Titanium's high-temperature elastic constants through the hcp–bcc phase transformation, Acta Mater. **52**, 2075 (2004).

[13] H. Ogi, K. Sato, T. Asada, and M. Hirao, Complete mode identification for resonance ultrasound spectroscopy, J. Acoust. Soc. Am. **112**, 2553 (2002).

[14] H. Ogi, N. Nakamura, K. Sato, M. Hirao, and S. Uda, Elastic, anelastic, and piezoelectric coefficients of langasite: Resonance ultrasound spectroscopy with laser-Doppler interferometry, IEEE Trans. Ultrason., Ferroelectr., Frequency Control **50**, 553 (2003).

[15] H. Ogi, M. Fukunaga, M. Hirao, and H. Ledbetter, Elastic constants, internal friction, and piezoelectric coefficient of α-TeO_2, Phys. Rev. B **69**, 024104 (2004).

[16] K. Adachi, H. Ogi, N. Takeuchi, N. Nakamura, H. Watanabe, T. Ito, and Y. Ozaki, Unusual elasticity of monoclinic β - Ga_2O_3, J. Appl. Phys. **124**, 085102 (2018).

[17] S. Ghosh, M. Matty, R. Baumbach, E. D. Bauer, K. A. Modic, A. Shekhter, J. A. Mydosh, E.-A. Kim, and B. J. Ramshaw, One-component order parameter in URu_2Si_2 uncovered by resonant ultrasound spectroscopy and machine learning, Sci. Adv. **6**, eaaz4074 (2020).

[18] W. Yang, S. Sun, J. Hu, L. Tang, L. Qin, Z. Li, and W. Luo, Deep learning model as an inversion tool for resonant ultrasound spectroscopy of piezoelectric materials, Appl. Phys. Lett. **120**, 184101 (2022).

[19] H. Ren, Q. Zhang, Z. Wang, G. Zhang, H. Liu, W. Guo, S. Mukamel, and J. Jiang, Machine learning recognition of protein secondary structures based on two-dimensional spectroscopic descriptors, Proc. Nat. Acad. Sci. **119**, e2202713119 (2022).

[20] M. Blackman, On anomalous vibrational spectra, Proc. Roy. Soc. Lond. **164**, 62 (1938).

[21] H. Ledbetter, *Blackman Diagrams and Elastic-Constant Systematics in Handbook of Elastic Properties of Solids, Liquids, and Gases II*, edited by M. Levy, H. Bass, and R. Stern (Academic Press, 2001), p. 57.

[22] See Supplemental Material at http://link.aps.org/supplemental/10.1103/PhysRevApplied.20.034048 for details of elasticity parameter $\tilde{C}$, Supplemental Figs. S1–S4, and Supplemental Tables S1–S8.

[23] H. Ogi, T. Ohmori, N. Nakamura, and M. Hirao, Elastic, anelastic, and piezoelectric coefficients of α-quartz determined by resonance ultrasound spectroscopy, J. Appl. Phys. **100**, 053511 (2006).

[24] K. He, X. Zhang, S. Ren, and J. Sun, in *2016 IEEE Conference on Computer Vision and Pattern Recognition (CVPR)* (2016), p. 770.

[25] N. Nakamura, H. Ogi, and M. Hirao, Elastic, anelastic, and piezoelectric coefficients of GaN, J. Appl. Phys. **111**, 013509 (2012).

[26] J. R. Neighbours and G. A. Alers, Elastic constants of silver and gold, Phys. Rev. **111**, 707 (1958).

[27] H.-G. von Purwins, R. Labusch, and P. Haasen, Elastische einkristallkonstanten von silberlegierungen, Z. fur Metallkd. **57**, 867 (1966).

[28] D. S. Tannhauser, L. J. Bruner, and A. W. Lawson, Temperature variation of the elastic constants of AgBr, Phys. Rev. **102**, 1276 (1956).

[29] R. F. S. Hearmon, The elastic constants of anisotropic materials II, Adv. Phys. **5**, 323 (1956).

[30] P. M. Sutton, The variation of the elastic constants of crystalline aluminum with temperature between 63°K and 773°K, Phys. Rev. **91**, 816 (1953).

[31] D. I. Bolef and M. Menes, Elastic constants of single-crystal aluminum antimonide, J. Appl. Phys. **31**, 1426 (1960).

[32] B. Golding, S. C. Moss, and B. L. Averbach, Composition and pressure dependence of the elastic constants of gold-nichel alloys, Phys. Rev. **158**, 637 (1967).

[33] R. F. S. Hearmon, The elastic constants of anisotropic materials, Rev. Mod. Phys. **18**, 409 (1946).

[34] K.-O. Park and J. M. Sivertsen, Elastic constants and attenuation changes in annealed BaO crystals, Phys. Lett. **55A**, 62 (1975).

[35] K. S. Aleksandrov and T. V. Ryzhova, The elastic properties of crystals, Sov. Phys., Crystallogr. **6**, 228 (1961).

[36] H. J. McSkimin and D. G. Thomas, Elastic moduli of cadmium telluride, J. Appl. Phys. **33**, 56 (1962).

[37] J. Gump, H. Xia, M. Chirita, R. Sooryakumar, M. A. Tomaz, and G. R. Harp, Elastic constants of face-centered-cubic cobalt, J. Appl. Phys. **86**, 6005 (1999).

[38] N. Uchida and S. Saito, Elastic constants and acoustic absorption coefficients in MnO, CoO, and NiO single crystals at room temperature, J. Acoust. Soc. Am. **51**, 1602 (1972).

[39] D. I. Bolef and J. de Klerk, Anomalies in the elastic constants and thermal expansion of chromium single crystals, Phys. Rev. **129**, 1063 (1963).

[40] W. C. Overton and Jr. J. Gaffney, Temperature variation of the elastic constants of cubic elements. I. Copper, Phys. Rev. **98**, 969 (1955).

[41] S. Siegel, The variation of the principal elastic moduli of Cu_3Au with temperature, Phys. Rev. **57**, 537 (1940).

[42] J. R. Neighbours and C. S. Smith, The elastic constants of copper alloys, Acta Metal. **2**, 591 (1954).

[43] R. E. Schmunk and C. S. Smith, Elastic constants of copper-nickel alloys, Acta Metal. **8**, 396 (1960).

[44] J. A. Rayne, Elastic constants of α-brasses: Room-temperature variation with solute concentration, Phys. Rev. **112**, 1125 (1958).

[45] H. M. Rosenberg and J. K. Wigmore, The elastic constants of potassium magnesium fluoride, Phys. Lett. **24A**, 317 (1967).

[46] J. A. Rayne and B. S. Chandrasekhar, Elastic constants of iron from 4.2 to 300°K, Phys. Rev. **112**, 1714 (1961).

[47] H. J. Leamy, E. D. Gibson, and F. X. Kayser, The elastic stiffness coefficients of iron-aluminium alloys – I Experimental results and thermodynamic analysis, Acta Metal. **15**, 1827 (1967).

[48] J. R. Drabble and A. J. Brammer, Third order elastic constants of gallium arsenide, Solid State Commun. **4**, 467 (1966).

[49] R. Weil and W. O. Groves, The elastic constants of gallium phosphide, J. Appl. Phys. **39**, 4049 (1968).

[50] H. J. McSkimin, A. Jayaraman, P. Andreatch, and Jr. T. B. Bateman, Elastic moduli of gallium antimonide under pressure and the evaluation of compression to 80 kbar, J. Appl. Phys. **39**, 4127 (1968).

[51] G. W. Shannette and J. F. Smith, Single-crystalline elastic constants of $ZrCo_2$ and $HfCo_2$ in the temperature range 4.2°–300°K, J. Appl. Phys. **40**, 79 (1969).

[52] T. Alper and G. A. Saunders, The elastic constants of mercury telluride, J. Phys. Chem. Solids **28**, 1637 (1967).

[53] D. Gerlich, Low-temperature elastic constants of indium arsenide, J. Appl. Phys. **35**, 3062 (1964).

[54] F. S. Hickernell and W. R. Gayton, Elastic constants of single-crystal indium phosphide, J. Appl. Phys. **37**, 462 (1966).

[55] R. F. Potter, Elastic moduli of indium antimonide, Phys. Rev. **103**, 47 (1956).

[56] K. M. Koliwad, P. B. Ghate, and A. L. Ruoff, Pressure derivatives of the elastic constants of NaBr and KF, Phys. Stat. Sol. **21**, 507 (1967).

[57] L. C. Davis, W. B. Whitten, and G. C. Danielson, Elastic constants and calculated lattice vibration frequencies of Mg_2Sn, J. Phys. Chem. Solids **28**, 439 (1967).

[58] C. H. Cheng, The elastic constants of MgAg and $MgCu_2$ single crystals, J. Phys. Chem. Solids **28**, 413 (1967).

[59] M. F. Lewis, Elastic constants of magnesium aluminate spinel, J. Acoust. Soc. Am. **40**, 728 (1966).

[60] D. W. Oliver, The elastic moduli of MnO, J. Appl. Phys. **40**, 893 (1969).

[61] D. I. Bolef and J. de Klerk, Elastic constants of single-crystal Mo and W between 77° and 500°K, J. Appl. Phys. **33**, 2311 (1962).

[62] D. L. Davidson and F. R. Brotzen, Elastic constants of molybdenum-rich rhenium alloys in the temperature range −190 °C to +100 °C, J. Appl. Phys. **39**, 5768 (1968).

[63] M. A. Durand, The temperature variation of the elastic moduli of NaCl, KCl, and MgO, Phys. Rev. **50**, 449 (1936).

[64] R. Viswanathan, Elastic constants of sodium chlorate single-crystals by pulse-echo method, J. Appl. Phys. **37**, 884 (1966).

[65] J. T. Lewis, A. Lehoczky, and C. V. Briscoe, Elastic constants of the alkali halides at 4.2°K, Phys. Rev. **161**, 877 (1967).

[66] P. E. Armstrong, J. M. Dickinson, and H. L. Brown, Temperature dependence of the elastic stiffness coefficients of niobium (columbium), Trans. Metal. Soc. AIME **236**, 1404 (1966).

[67] K. R. Keller and J. J. Hanak, Lattice softening in single crystal Nb_3Sn, Phys. Lett. **21**, 263 (1966).

[68] R. J. Wasilewski, Elastic constants and Young's modulus of NiAl, Trans. Metal. Soc. AIME **236**, 455 (1966).

[69] E. Z. Vintaikin, X-ray determination of the elastic constants of pure nickel and its alloy with aluminum, Sov. Phys.-Dokl. **11**, 91 (1966).

[70] S. G. Epstein and O. N. Carlson, The elastic constants of nickel-copper alloy single crystals, Acta Metal. **13**, 487 (1965).

[71] J. H. Wasilik and M. L. Wheat, Elastic constants of cubic lead fluoride at room temperature, J. Appl. Phys. **36**, 791 (1965).

[72] J. A. Rayne, Elastic constants of palladium from 4.2–300°K, Phys. Rev. **118**, 1545 (1960).

[73] N. G. Einspruch and L. T. Claiborne, Elastic constants of a (73.8% Ni–26.2% Fe) ferromagnetic alloy, J. Appl. Phys. **35**, 175 (1964).

[74] R. E. MacFarlane, J. A. Rayne, and C. K. Jones, Anomalous temperature dependence of shear modulus c_{44} for platinum, Phys. Lett. **18**, 91 (1965).

[75] M. Ghafelehbashi, D. P. Dandekar, and A. L. Ruoff, Pressure and temperature dependence of the elastic constants of RbCl, RbBr, and RbI, J. Appl. Phys. **41**, 652 (1970).

[76] H. J. McSkimin, P. Andreatch, Jr., Elastic moduli of silicon vs hydrostatic pressure at 25.0 °C and −195.8 °C, J. Appl. Phys. **35**, 2161 (1964).

[77] D. Gerlich, Elastic constants of strontium fluoride between 4.2 and 300°K, Phys. Rev. **136**, A1366 (1964).

[78] D. L. Johnston, P. H. Thrasher, and R. J. Kearney, Elastic constants of SrO, J. Appl. Phys. **41**, 427 (1970).
[79] J. B. Wachtman, Jr. M. L. Wheat, and S. Marzullo, A method for determining the elastic constants of a cubic crystal from velocity measurements in a single arbitrary direction; application to $SrTiO_3$, J. Res. Natl. Bur. Stand. **67A**, 193 (1963).
[80] D. I. Bolef, Elastic constants of single crystals of the bcc transition elements V, Nb, and Ta, J. Appl. Phys. **32**, 100 (1961).
[81] P. E. Armstrong, O. N. Carlson, and J. F. Smith, Elastic constants of thorium single crystals in the range 77–400°K, J. Appl. Phys. **30**, 36 (1959).
[82] P. M. Macedo, W. Capps, J. B. Wachtman, Jr., Elastic constants of single crystal ThO_2 at 25 °C, J. Amer. Ceram. Soc. **47**, 651 (1964).
[83] S. von Haussühl, Elastische eigenschaften von Kristallen des CsCl-types, Acta Cryst. **13**, 685 (1960).
[84] L. J. Graham, H. Nadler, and R. Chang, Elastic constants of UC, J. Appl. Phys. **34**, 1572 (1963).
[85] J. B. Wachtman, Jr. M. L. Wheat, H. J. Anderson, and J. L. Bates, Elastic constants of single crystal UO_2 at 25 °C, J. Nucl. Mat. **16**, 39 (1965).
[86] G. A. Alers, Elastic moduli of vanadium, Phys. Rev. **119**, 1532 (1960).
[87] D. Berlincourt, H. Jaffe, and L. R. Shiozawa, Electroelastic properties of the sulfides, selenides, and tellurides of zinc and cadmium, Phys. Rev. **129**, 1009 (1963).
[88] P. Sedlák, H. Seiner, M. Landa, V. Novák, P. Šittnere, and L. Mañosa, Elastic constants of bcc austenite and 2H orthorhombic martensite in CuAlNi shape memory alloy, Acta Mater. **53**, 3643 (2005).
[89] J. Smith and C. L. Arbogast, Elastic constants of single crystal beryllium, J. Appl. Phys. **31**, 99 (1960).
[90] Y. A. Change and L. Himmel, Elastic constants of cadmium from 300° to 575°K, J. Appl. Phys. **37**, 3787 (1966).
[91] E. S. Fisher and D. Dever, Temperature dependence of elastic moduli of ruthenium, rhenium, cobalt, dysprosium, and erbium; a study of the elastic anisotropy - phase transformation relationship, Trans. Metal. Soc. AIME **239**, 48 (1967).
[92] H. Fukuda, A. Nagakubo, S. Usami, M. Ikeda, M. Imanishi, M. Yoshimura, Y. Mori, K. Adachi, and H. Ogi, Determination of the electron trap level in Fe-doped GaN by phonon-assisted conduction phenomenon, Appl. Phys. Express **15**, 071003 (2022).
[93] E. S. Fisher and C. J. Renken, Single-crystal elastic moduli and the hcp → bcc transformation in Ti, Zr, and Hf, Phys. Rev. **135**, A482 (1964).
[94] L. J. Slutsky and C. W. Garland, Elastic constants of magnesium from 4.2°K to 300°K, Phys. Rev. **107**, 972 (1957).
[95] M. L. Shepard and J. F. Smith, Elastic constants of rhenium single crystals in the temperature range 4.2°–298°K, J. Appl. Phys. **36**, 1447 (1965).
[96] J. F. Smith and J. A. Gjevre, Elastic constants of yttrium single crystals in the temperature range 4.2–400°K, J. Appl. Phys. **31**, 645 (1960).
[97] R. Hill, The elastic behaviour of a crystalline aggregate, Proc. Phys. Soc. A **65**, 349 (1952).